Sensors and Materials, Vol. 38, No. 2 (2026) 593–602
MYU Tokyo

S & M 4327

Luminescence Properties of Broadband Near-infrared Luminescent Material $Ca_5Ga_6O_{14}:Cr^{4+}$

Aunsaya Eksatit,[1] Takayuki Nakanishi,[1*] Takuya Ohmi,[1] Akihiro Nakanishi,[1] Naoto Hirosaki,[1] Takashi Takeda,[1] Jian Xu,[2,3] Jumpei Ueda,[4] and Koji Morita[1**]

[1]Research Center for Electronic and Optical Materials, National Institute for Materials Science, 1-1 Namiki, Tsukuba, Ibaraki 305-0044, Japan
[2]Graduate School of Human and Environmental Studies, Kyoto University, Kyoto, Kyoto 606-8316, Japan
[3]Graduate School of Global Environmental Studies (GSGES), Kyoto University, Kyoto, Kyoto 606-8501, Japan
[4]Graduate School of Advanced Science and Technology, Japan Advanced Institute of Science and Technology, 1-1 Asahidai, Nomi, Ishikawa 923-1292, Japan

(Received October 30, 2025; accepted December 10, 2025)

Keywords: Cr^{4+} photoluminescence, broadband NIR emission, NIR phosphors

Broadband near-infrared-II (NIR-II) covered phosphors are crucial for LED applications such as biological imaging and optical sensing. In this study, $Ca_5Ga_{6-x}O_{14}$: xCr phosphors, where x represents the molar concentration of Cr^{4+} substituting Ga sites, were synthesized with x values of 0.0001, 0.0005, 0.005, 0.01, 0.02, 0.03, and 0.04 using a conventional solid-state reaction. X-ray diffraction showed that the main targeted phase was predominantly observed for Cr doping levels below x = 0.001. Optical characterizations revealed that the optimized phosphor (x = 0.0005) exhibited the most intense and broad NIR emission (1150–1600 nm, peak at 1330 nm) by 650 nm excitation, originating from the spin-allowed $^3T_2 \rightarrow {}^3A_2$ transition of tetrahedrally coordinated Cr^{4+} ions. Low-temperature photoluminescence further elucidated the energetic and crystal field environment of Cr^{4+}. These findings demonstrate that $Ca_5Ga_6O_{14}$ is an efficient host for Cr^{4+}-doped NIR-II phosphors, offering insights for the design of next-generation luminescent materials.

1. Introduction

NIR phosphors have significant potential for advanced applications such as biological imaging and materials analysis, driving demand for efficient broadband NIR emitters.[1,2] Among these, phosphor groups centered on Cr ions as the luminescent core are being investigated as promising materials for near-infrared LEDs exhibiting broad emission.[3,4] Conventional Cr^{3+}-doped phosphors are mainly suitable for NIR-I emission (650–950 nm), but achieving the superior performance required in the NIR-II spectral region (1000–1700 nm) motivates the development of Cr^{4+}-doped materials.[5–11] A major challenge in this field is the natural preference of chromium ions for the Cr^{3+} oxidation state in octahedral coordination, whereas Cr^{4+} luminescence requires a suitable host offering tetrahedral sites.[12,13] In this study,

*Corresponding author: e-mail: NAKANISHI.Takayuki@nims.go.jp
**Corresponding author: e-mail: MORITA.Koji@nims.go.jp
https://doi.org/10.18494/SAM6005

ISSN 0914-4935
https://myukk.org/

$Ca_5Ga_6O_{14}$ with a melilite-type gallate framework consisting of [GaO_4] tetrahedral layers (Fig. 1) was employed as the host crystal, as its structure facilitates the effective substitution of Cr^{4+} ions and enhances their luminescent properties. In this work, we investigate the crystal structure and photoluminescence properties of Cr^{4+}-doped $Ca_5Ga_6O_{14}$ phosphors, providing insights into the design and optimization of host matrices for efficient broadband NIR-II emission, and advancing the development of next-generation NIR materials.

2. Data, Materials, and Methods

2.1 Sample preparation

A series of Cr^{4+}-doped phosphors with the general formula $Ca_5Ga_{6-x}O_{14}$: xCr (x = 0.0001, 0.0005, 0.005, 0.02, and 0.03) are synthesized via a solid-state reaction method. First, stoichiometric amounts of high-purity $CaCO_3$ (99.99%) and Ga_2O_3 (99.99%) powders (Kojundo Chemical Laboratory Co., Ltd., Japan) were weighed, and appropriate amounts of Cr_2O_3 powder (99.9%, Kojundo Chemical Laboratory Co., Ltd., Japan) were added to achieve the desired Cr doping concentrations. The powder was homogeneously mixed in an agate mortar for 30 min. The powder mixture was then preheated in a furnace at 700 °C for 3 h to remove volatile components and initiate preliminary reactions. Following the preheating step, the powders were calcined at 1300 °C for 10 h in oxidation atmosphere. After calcination, the samples were allowed to cool naturally to room temperature and then ground into fine powders for the following characterizations.

2.2 Characterization

X-ray diffraction (XRD) was performed using a SmartLab X-ray diffractometer (Rigaku Co., Ltd.) with Cu $K\alpha_1$ radiation (λ = 1.54059 Å, 40 kV, and 40 mA) over a 2θ range of 5–80° at a scanning rate of 0.01°/min. The obtained XRD patterns were analyzed by Le Bail refinement using the Jana2006 program.[15] A pseudo-Voigt function was employed to fit the peak profiles.

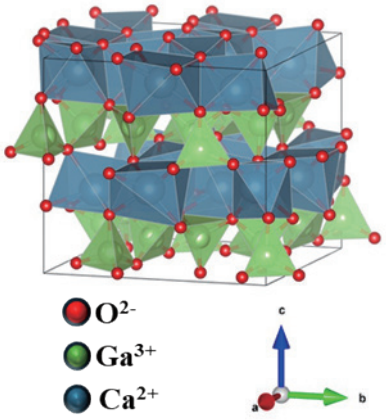

Fig. 1. Crystal structure of $Ca_5Ga_6O_{14}$ host.[14]

The refinements were performed over a 2θ range of 5–65°. A two-phase model consisting of $Ca_5Ga_6O_{14}$ (orthorhombic, $Cmc2_1$) as the main phase and $Ca_3Ga_4O_9$ (orthorhombic, *Cmm*2) as a minor secondary phase was employed to improve the fitting quality. The background was fitted using a polynomial function, and the peak-shape parameters, zero shift, scale factors, and lattice parameters were refined. Three times the standard deviation (3σ) obtained from the most converged 10 refinement cycles was empirically taken as the error bar. Diffuse reflectance spectra (DRS) were recorded with a UV–visible spectrophotometer (SHIMADZU UV-3600), calibrated with $BaSO_4$ (Nacalai Tesque, Inc.) as the reference standard. The X-ray absorption near-edge structure (XANES) spectrum of the K edge of Cr in fluorescent mode was measured using the BL-9A beamline at KEK, Japan. X-ray energy selection was achieved using a silicon (111) double-crystal monochromator. A 7-element solid-state detector (7-element SSD) was used owing to the low concentration of Cr. A vanadium metal filter was set in front of the SSD for the band-pass filter. The XANES spectra were measured within the range of 5955–6060 eV with an increment of 0.35 eV. After the XANES measurement, the background process was conducted using Athena software. Photoluminescence (PL) and photoluminescence excitation (PLE) spectra were measured using a near-infrared spectrofluorometer (FP-8700, JASCO) equipped with a xenon lamp, and the excitation wavelength was set to 650 nm. Emission spectra were collected in the range of 1100–1600 nm. Low-temperature PL and PLE measurements were conducted at 6 K in a cryostat. PLE spectra in the near-infrared region were obtained using a monochromator equipped with a tungsten halogen lamp as the excitation source, whereas PL spectra were measured with a photoluminescence spectrometer (MCPD-9800, Otsuka Electronics).

3. Results and Discussion

3.1 Phase composition analysis

Figure 2(a) shows the XRD patterns of synthesized $Ca_5Ga_{6-x}O_{14}$: *x*Cr samples with various Cr doping concentrations of $x = 0$–0.03 and the simulated pattern calculated with the reported structure of $Ca_5Ga_6O_{14}$ (ICSD 62324).[16] All samples were identified as $Ca_5Ga_6O_{14}$ as the main phase with an orthorhombic crystal system (space group $Cmc2_1$). The samples with $x = 0.001$–0.03 contained a small amount of $Ca_3Ga_4O_9$ (ICSD 12172)[17] as a secondary phase with an orthorhombic crystal system (space group *Cmm2*), whereas the samples with $x = 0$, 0.0001 and 0.0005 were obtained as a single phase of the target compound $Ca_5Ga_6O_{14}$. All diffraction patterns exhibit strong preferred orientation along the (002) plane, which is consistent with the layered feature of the $Ca_5Ga_6O_{14}$ crystal structure. These results demonstrate that the primary $Ca_5Ga_6O_{14}$ phase can be reliably obtained at low to moderate Cr concentrations, whereas phase purity decreases progressively with increasing Cr content owing to the formation of secondary phases.

Le Bail refinements were performed for the selected samples with $x = 0.0005$, 0.005, 0.02, and 0.03 to determine the lattice parameters as a function of Cr doping amount (x). Figures 2(b) and 2(c) show a representative fitting profile for the $x = 0.0005$ ($Ca_5Ga_{5.995}O_{14}$: 0.0005Cr)

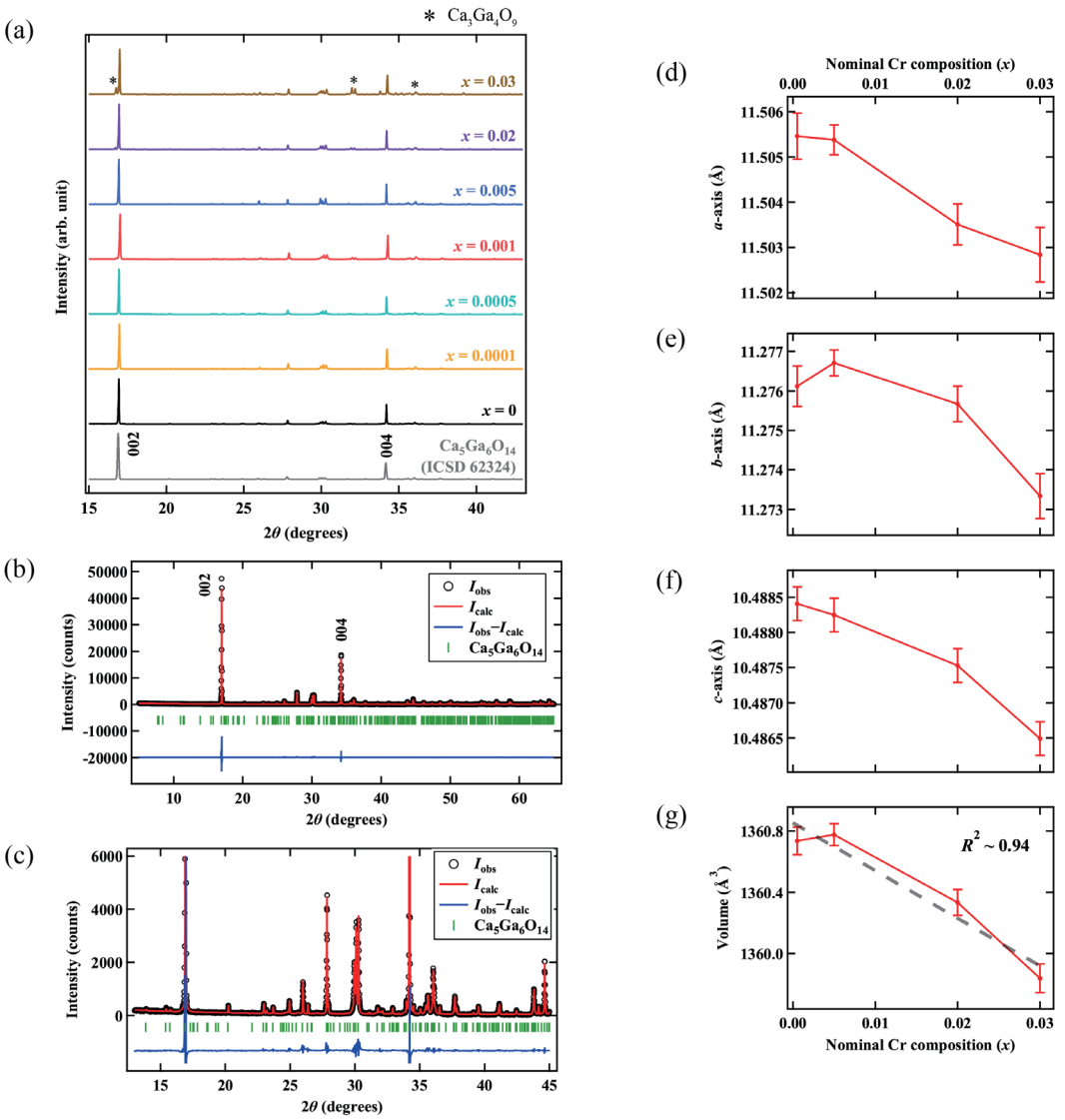

Fig. 2. (a) XRD patterns of Ca_5Ga_6-xO_{14}: xCr (x = 0–0.03) samples, along with the simulated pattern based on the reported structure of $Ca_5Ga_6O_{14}$,[15] taking into account the preferred orientation along the (002) plane. (b, c) Representative results of Le Bail refinement of the powder XRD pattern of $Ca_5Ga_{5.995}O_{14}$: 0.0005Cr. The black markers, red line, and blue line represent the observed, calculated, and difference intensities, respectively, and green ticks show Bragg positions of $Ca_5Ga_{5.995}O_{14}$: 0.0005Cr. (d–g) Calculated lattice parameters and unit-cell volume of $Ca_5Ga_{6-x}O_{14}$: xCr (x = 0.0005, 0.005, 0.02, and 0.03). A dashed line in the unit-cell volume plot indicates the result of the linear fit. Error bars represent three times the standard deviation (3σ).

sample. Almost all reflections of $Ca_5Ga_6O_{14}$ were successfully indexed. Large differences remain at the high-intensity diffractions corresponding to the 002 and 004 indices owing to the strong preferred orientation. Although Rietveld refinement was also attempted to estimate the phase fraction of the $Ca_3Ga_4O_9$ impurity phase, good convergence could not be achieved owing to the strong preferred orientation of the $Ca_5Ga_6O_{14}$ main phase.

The plots of the calculated lattice parameters as a function of composition [Figs. 2(d)–2(g)] reveal a clear trend of decreasing lattice parameters and a contraction of the unit-cell volume

with increasing x. This lattice shrinkage supports the substitution of smaller Cr^{4+} ions (r_{ion} = 0.41 Å) for larger Ga^{3+} sites (r_{ion} = 0.47 Å).[18] Unexpectedly, no anisotropic changes in lattice parameters were observed, which are often observed in layered structures. The overall trend in the unit-cell volume follows Vegard's law. The linear fitting yields $R^2 \sim 0.94$, indicating good agreement. However, considering the appearance of impurity phases at $x \geq 0.001$, the actual incorporated composition may deviate from the nominal one in this range.

3.2 Valence state and optical properties

The UV–vis DRS were analyzed to determine the oxidation states of the chromium ions in the Cr-doped $Ca_5Ga_6O_{14}$ phosphors. As shown in Fig. 3(a), the DRS display absorption features characteristic of different chromium oxidation states: Cr^{4+} exhibits three distinct bands including a weak band at 400–500 nm [$^3A_2 \rightarrow {}^3T_1(^3P)$] and a broad band at 550–1170 nm ($^3A_2 \rightarrow {}^3T_2$), while a peak at 370 nm indicates the presence of Cr^{6+} (due to oxygen-to-Cr^{6+} charge transfer).[19–21] With increasing Cr concentration, the absorption intensity is notably enhanced, suggesting the higher mixed-valence state at a higher level of doping.

To further elucidate the local environment of Cr ions, XANES measurements were performed [Figs. 3(b) and 3(c)]. The measurements were carried out using the $Ca_5Ga_{5.995}O_{14}$: 0.0005Cr

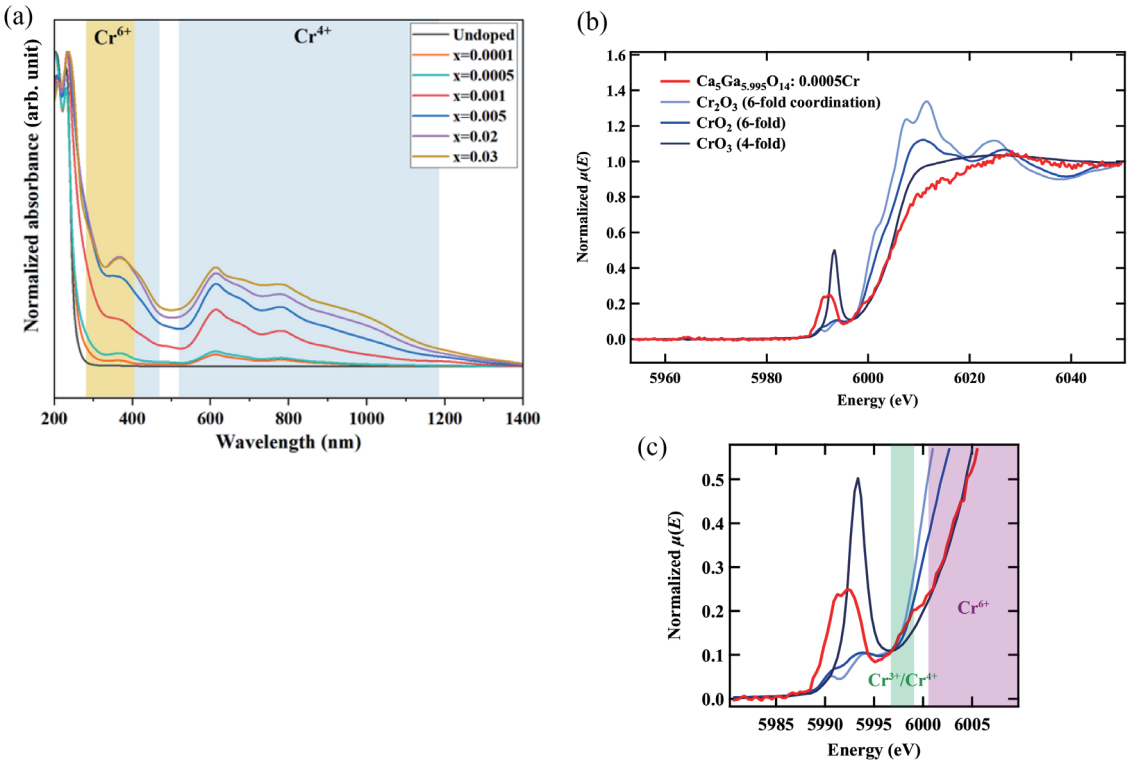

Fig. 3. (a) UV–vis absorption spectra of $Ca_5Ga_{6-x}O_{14}$: xCr (0–0.03) (b, c) Normalized XANES spectra of $Ca_5Ga_{5.995}O_{14}$: 0.0005Cr and reference compounds (Cr_2O_3, CrO_2, and CrO_3) corresponding to Cr^{3+}, Cr^{4+}, and Cr^{6+}, respectively. Note that Cr_2O_3 and CrO_2 are octahedrally (6-fold) coordinated, whereas CrO_3 is tetrahedrally (4-fold) coordinated.

sample in order to minimize phase impurities. As shown in the enlarged spectrum in Fig. 3(c), $Ca_5Ga_{5.995}O_{14}$: 0.0005Cr exhibits a distinct pre-edge peak, which is typically observed with strong intensity when Cr ions occupy tetrahedral coordination sites.[22] This pre-edge feature therefore indicates that Cr ions preferentially occupy the Ga^{3+} tetrahedral sites in the $Ca_5Ga_6O_{14}$ lattice. The pre-edge peak shows a slight shift toward lower energy compared with the CrO_3 reference, suggesting the presence of Cr ions with a lower oxidation state than Cr^{6+}.

In contrast, the main absorption edge of the sample largely overlaps with that of Cr^{6+} around 6000–6005 eV, consistent with the DRS results. Additionally, as shown in the rising-edge region of the main absorption edge [Fig. 3(c)], partial overlap with the CrO_2 and Cr_2O_3 references can be observed around 5996–5998 eV, implying the coexistence of multiple valence states. Further investigations using high-resolution XANES measurements and purified reference samples will enable a more quantitative analysis.

3.3 Photoluminescence properties

At room temperature, the PL and PLE properties of the $Ca_5Ga_{6-x}O_{14}$: *x*Cr phosphor are affected by the Cr doping concentration (x = 0 to 0.03), as seen in Fig. 4. Under 650 nm excitation, the phosphor exhibits a broad NIR emission from 1150 to 1600 nm, peaked at 1330 nm, which is attributed to the spin-allowed $^3T_2 \rightarrow {}^3A_2$ transition of the Cr^{4+} ions occupying tetrahedral sites. The PLE spectrum monitored at 1330 nm shows a main peak at 670 nm [$^3A_2 \rightarrow {}^3T_1(^3F)$] and a weak peak at 500 nm [$^3A_2 \rightarrow {}^3T_1(^3P)$].[10] The luminescence intensity initially increases with increasing Cr content and reaches a maximum at x = 0.0005, then gradually decreases due to energy transfer between Cr ions, which leads to concentration quenching. While diffuse reflectance spectra and XANES measurements indicate the presence of multiple Cr valence states in $Ca_5Ga_{6-x}O_{14}$: *x*Cr, no distinct excitation or emission bands attributable to Cr^{3+} or Cr^{6+} are observed in the PL and PLE spectra under 650 nm excitation. The observed spectral features are consistent with the characteristic transitions of Cr^{4+}, confirming Cr^{4+} as the primary luminescent center. Furthermore, at this optimal doping, the internal quantum, external quantum, and absorption efficiencies of $Ca_5Ga_{5.9995}O_{14}$:0.0005Cr^{4+} were evaluated, yielding values of 2.39, 1.42, and 59.34%, respectively. Although the sample exhibits strong characteristic emission from Cr^{4+} centers and substantial light absorption, the relatively low quantum efficiencies highlight the need for further optimization to improve practical performance in potential applications.

Figure 5(a) shows the low-temperature PL and PLE spectra of $Ca_5Ga_{5.9995}O_{14}$:0.0005Cr^{4+} measured at 6 K to determine the energy levels. Several excitation peaks are observed at approximately 700, 790, 880, 1020, 1120, 1175, 1200, and 1215 nm, accompanied by a zero-phonon line (*ZPL*) near 1225 nm, which is observed in the PL spectra. At this temperature, phonon oscillations within the crystal lattice are suppressed, thus maintaining the distinct characteristics of the transitions. As compared with the low-temperature spectrum, the PL intensity at room temperature markedly decreased, indicating the strong thermal quenching behavior of the Cr^{4+} centers. A Tanabe–Sugano diagram shown in Fig. 5(b) illustrates the energy levels of Cr^{4+} in a tetrahedral coordination environment. This diagram demonstrates the

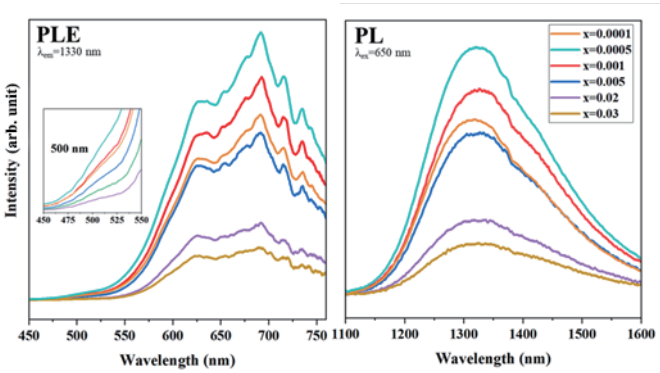

Fig. 4. Concentration-dependent PLE and PL spectra of $Ca_5Ga_{5.995}O_{14}$: 0.0005Cr.

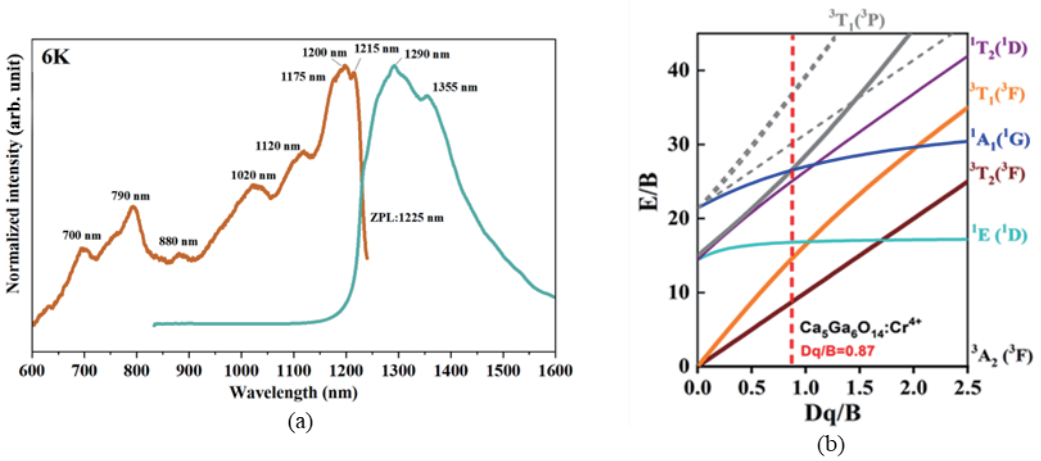

Fig. 5. (a) PLE and PL spectra of $Ca_5Ga_{5.995}O_{14}$:0.0005Cr obtained at 6 K. (b) Tanabe–Sugano diagram of Cr^{4+} in the tetrahedral coordination environment.

relationship between electronic state energies and crystal field strength (D_q/B). By analyzing these diagrams, the energies of spin-allowed and spin-forbidden transitions can be predicted. Since the emission characteristics of Cr^{4+} are closely related to the crystal field strength, the crystal field parameter (D_q) can be calculated from the energy of the zero-phonon line (ZPL) as follows:

$$10D_q = E(ZPL). \tag{1}$$

The crystal field strength (D_q/B) for a tetrahedral configuration can be calculated as[14]

$$\frac{D_q}{B} = \frac{15\left(\frac{\Delta E}{D_q} - 8\right)}{(\Delta E / D_q)^2 - 10(\Delta E / D_q)}, \tag{2}$$

where B is the Racah parameter and ΔE is defined as

$$\Delta E = E[^3A_2 \rightarrow {}^3T_1(^3P)] - E[^3A_2 \rightarrow {}^3T_1(^3F)]. \quad (3)$$

The transition energies of $^3A_2 \rightarrow {}^3T_1(^3P)$ and $^3A_2 \rightarrow {}^3T_1(^3F)$ levels in $Ca_5Ga_{5.995}O_{14}$:0.0005 Cr^{4+} are indicated as $E[^3A_2 \rightarrow {}^3T_1(^3P)]$ and $E[^3A_2 \rightarrow {}^3T_1(^3F)]$, respectively. The wavenumbers for these transition energies are measured to be 20000 and 14492 cm^{-1}, respectively. The crystal field characteristics were estimated as follows: D_q = 819 cm^{-1}, B = 939 cm^{-1}, and D_q/B = 0.87. The intersection of the excited states of the $^3T_2$ and ^1E energy levels is defined by D_q/B = 1.6 in Tanabe–Sugano diagrams for tetrahedral coordination. The Cr^{4+}-doped phosphor exhibiting a D_q/B ratio below this threshold is considered to be in a weak crystal field, leading to electron transitions from $^3T_2$ to $^3A_2$, which result in broadband emission. $Ca_5Ga_{5.995}O_{14}$:0.0005 Cr^{4+}, with a crystal field strength of 0.87, is defined as a weak crystal field type. This leads to the occurrence of broadband emission.

For further investigation, the Huang–Rhys parameter (S) was studied to determine the strength of electron–phonon coupling in the phosphor material, allowing the thermal behavior on luminescence properties to be explained. S can be calculated as[23]

$$FWHM = 2.36\sqrt{S}\hbar\omega\sqrt{\coth\frac{\hbar\omega}{2kT}}, \quad (4)$$

where FWHM is the full width at half maximum of the emission peak, which is determined by fitting the PL spectra with Gaussian functions to enable the accurate extraction of linewidths, S is the Huang–Rhys parameter, $\hbar\omega$ is the effective phonon energy, k is the Boltzmann constant, and T is the absolute temperature. Practically, the equation can be simplified to[24]

$$FWHM^2 = 5.57 \times S \times (\hbar\omega)^2\left[1 + \frac{1}{\hbar\omega / 2kT}\right]. \quad (5)$$

From fitting the experimental FWHM values, the intercept (a) and slope (b) were determined to be a = 0.0154 and b = 0.3221, respectively.

$$FWHM^2 = a + \frac{b}{1/(2kT)} \quad (6)$$

The effective phonon energy (E_{ph}) was calculated as

$$E_{ph} = \frac{b}{a} = \frac{0.3221}{0.0154} = 0.0477\,\text{eV}. \quad (7)$$

The Huang–Rhys parameter was evaluated as

$$S = \frac{a}{5.57 \times E_{ph}^2} = \frac{0.0154}{5.57 \times (0.0477)^2} = 1.21 . \quad (8)$$

These results indicate moderate electron–phonon coupling in this phosphor.[23] The thermal quenching observed in $Ca_5Ga_6O_{14}$ is associated with this coupling strength, as it facilitates the interaction between excited electrons and lattice vibrations, promoting nonradiative relaxation pathways. Consequently, further elucidation of the thermal properties and quenching mechanisms in synthesized phosphors remains important for future research.

4. Conclusions

A broadband NIR phosphor, $Ca_5Ga_6O_{14}:Cr^{4+}$, was successfully synthesized via a solid-state reaction. The substitution of Cr^{4+} ions into the host lattice was confirmed by the UV–vis diffuse reflectance and photoluminescence measurements. Under 650 nm excitation, the optimized $Ca_5Ga_{5.995}O_{14}:0.0005Cr^{4+}$ phosphor exhibited a broad NIR-II emission band ranging from 1150 to 1600 nm peaked at 1330 nm. It is attributed to the spin-allowed $^3T_2 \rightarrow {}^3A_2$ transitions of Cr^{4+}, which serves as the luminescent center in this host lattice. Studies on low-temperature photoluminescence reveal that the emission intensity and spectral features are strongly affected by temperature. These results demonstrate that Cr^{4+}-doped $Ca_5Ga_6O_{14}$ is a promising host matrix for further expanding the understanding and discovery of efficient broadband NIR phosphors.

Acknowledgments

This work was supported by the Innovative Science and Technology Initiative for Security (Grant Number JPJ004596), ATLA, Japan. In addition, this work was partially supported by JSPS KAKENHI Grant Number 24K01589. XANES measurement was performed at the High Energy Accelerator Research Organization Photon Factory (KEK-PF; 2025G110).

References

1 K. B. Beć, J. Grabska, and C. W. Huck: Chem. Eur. J. **27** (2021) 5. https://doi.org/10.1002/chem.202002838
2 C. Pasquini: J. Braz. Chem. Soc. **14** (2003) 2. https://doi.org/10.1590/S0103-50532003000200006
3 S. Liu, Z. Wang, H. Cai, Z. Song, and Q. Liu: Inorg. Chem. Front. **7** (2020) 6. https://doi.org/10.1039/d0qi00063a
4 P. Dang, Y. Wei, D. Liu, G. Li, and J. Lin: Adv. Opt. Mater. **11** (2023) 3. https://doi.org/10.1002/adom.202201739
5 V. Rajendran, H. Chang, and R. S. Liu: Opt. Mater.: X. **1** (2019) 1. https://doi.org/10.1016/j.omx.2019.100011
6 Y. Zhou, X. Li, T. Seto, and Y. Wang: ACS Sustain. Chem. Eng. **9** (2021) 8. https://doi.org/10.1021/acssuschemeng.0c07946
7 T. Tan, S. Wang, J. Su, W. Yuan, H. Wu, R. Pang, C. Li, and H. Zhang: ACS Sustain. Chem. Eng. **10** (2022) 12. https://doi.org/10.1021/acssuschemeng.1c07054
8 S. Miao, Y. Liang, Y. Zhang, D. Chen, and X. J. Wang: ACS Appl. Mater. Interfaces. **13** (2021) 30. https://doi.org/10.1021/acsami.1c10490

9 H. Zhou, H. Cai, J. Zhao, Z. Song, and Q. Liu: Inorg. Chem. Front. **9** (2022) 9. https://doi.org/10.1039/d2qi00217e
10 S. Yuan, Z. Mu, L. Lou, S. Zhao, D. Zhu, and F. Wu: Ceram. Int. **48** (2022) 18. https://doi.org/10.1016/j.ceramint.2022.05.391
11 T. Nakanishi, M. Tsurui, J. Xu, N. Takahashi, T. Takeda, and N. Hirosaki: Sens. Mater. **33** (2021) 2227. https://doi.org/10.18494/sam.2021.3320
12 Y. Wang, G. Liu, and Z. Xia: Laser Photonics Rev. **18** (2024) 1. https://doi.org/10.1002/lpor.202300717
13 Q. Zhang, D. Liu, P. Dang, H. Lian, G. Li, and J. Lin: Laser Photonics Rev. **16** (2022) 2. https://doi.org/10.1002/lpor.202100459
14 A. I. Bilyi, V. A. Bruskov, J. N. Grin, P. J. Zavalij, V. V. Kravchishin, and A. E. Nosenko: Sov. Phys. Crystallogr. **31** (1986) 6.
15 V. Petříček, M. Dušek, and L. Palatinus: Z. Kristallogr. Cryst. Mater. **229** (2014) 5. https://doi.org/10.1515/zkri-2014-1737
16 B. V. Merinov, S. L. Londar, and Y. M. Zakharko: Sov. Phys. Crystallogr. **33** (1988) 1.
17 Y. Yasui, E. Niwa, M. Matsui, K. Fujii, and M. Yashima: Inorg. Chem. **58** (2019) 14. https://doi.org/10.1021/acs.inorgchem.9b01300
18 R. D. Shannon: Acta Crystallogr. A. **32** (1976) 5. https://doi.org/10.1107/S0567739476001551
19 C. Jousseaume, A. Kahn-Harari, D. Vivien, J. Derouet, F. Ribot, and F. Villain: J. Mater. Chem. **12** (2002) 5. https://doi.org/10.1039/b106707a
20 N. Majewska, Y. T. Tsai, X. Y. Zeng, M. H. Fang, and S. Mahlik: Chem. Mater. **35** (2023) 23. https://doi.org/10.1021/acs.chemmater.3c02466
21 D. Reinen, U. Kesper, M. Atanasov, and J. Roos: Inorg. Chem. **34** (1995) 1. https://doi.org/10.1021/ic00105a031
22 T. Yamamoto: X-Ray Spectrom. **37** (2008) 6. https://doi.org/10.1002/xrs.1103
23 G. Wei, P. Li, R. Li, Y. Wang, S. He, J. Li, Y. Shi, H. Suo, Y. Yang, and Z. Wang: Adv. Opt. Mater. **11** (2023) 24. https://doi.org/10.1002/adom.202301794
24 D. Hou, H. Lin, Y. Zhang, J.Y. Li, H. Li, J. Dong, Z. Lin, and R. Huang: Inorg. Chem. Front. **8** (2021) 9. https://doi.org/10.1039/d0qi01524e